

The Afterglow of the August 17th 2017 Binary Neutron Star Merger Multi-messenger Event

Raphaël Duque

Summary

Résumé

Contents

I	Introduction	4
1	MMT170817 – a historical event	4
2	Description of the multi-messenger observations	4
2.1	GW170817: gravitational waves from the inspiral phase	4
2.2	GRB170817A: the gamma-ray burst	4
2.3	AT 2017gfo: the kilonova	5
2.4	The afterglow signal	5
3	Goal of this work and the afterglow of MMT170817 as an insight on the merger event	5
II	Modelling the afterglow of MMT170817	7
4	The physics of afterglows: deceleration dynamics, radiation and astronomical observables	7
4.1	Relativistic deceleration	7
4.2	Synchrotron radiation and self-absorption	9
4.3	Derivation of the astronomical observable: flux density	10
4.4	An illustration of some predicted light curves	11
5	The afterglow of MMT170817: modelling and results	11
5.1	Choice and reduction of multi-wavelength data	11
5.2	Can the afterglow come from a post-GRB relativistic jet?	12
5.3	A quasi-spherical remnant	14
5.4	Conclusion	14
6	Discussion around the results from the afterglow modelling	14
6.1	General discussion	14
6.2	The external medium	16
6.3	What of the standard relativistic jet?	17
III	Perspectives on the electromagnetic counterparts of binary neutron star mergers	22
7	Future rates of events and counterparts	22
8	Insights on other astronomical observables	22
9	Open questions	22

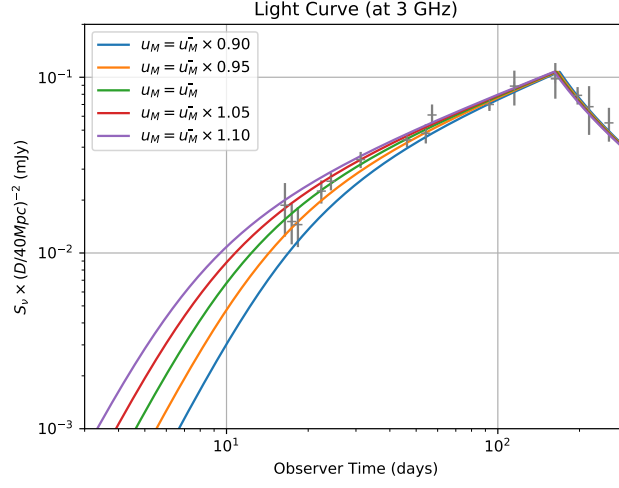


Figure 1: A nice figure

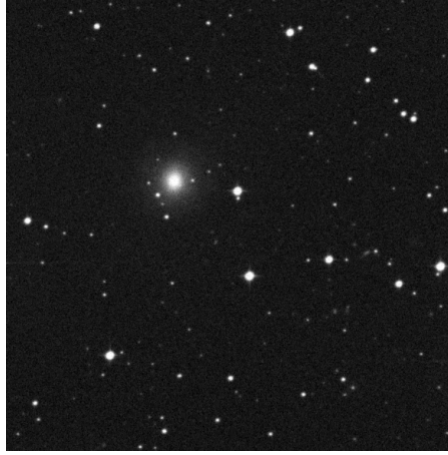


Figure 2: Spectrogram of a combination of both LIGO interferometers' data from GW170817 ([?]). Note the non-detection of a ring-down signal.

Part I

Introduction

1 MMT170817 – a historical event

2 Description of the multi-messenger observations

2.1 GW170817: gravitational waves from the inspiral phase

2.2 GRB170817A: the gamma-ray burst

As illustrated in figure 2.2, GRB170817A is an outlier of the E_p - L_{iso} relation, also known as the Yonetoku relation ([?]). In this relation, E_p and L_{iso} are the peak photon energy and isotropic equivalent luminosity of the burst at its peak.

This observation is the first which hints to the *atypical* character of GRB170817A.

Using a simple calculation to estimate the E_p and L_{iso} values which would have been observed from different angles, it appears that this event is an outlier of the Yonetoku relation regardless of the viewing angle.

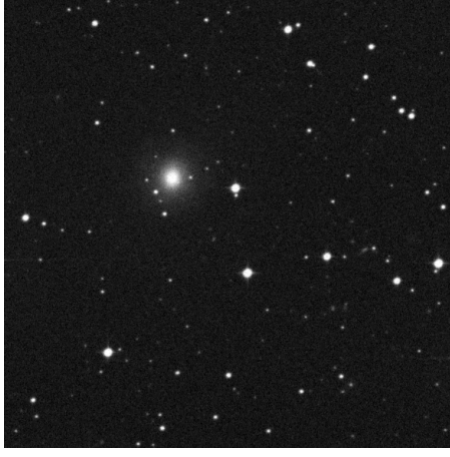


Figure 3: The Yonetoku relation for the Swift BAT 4 catalog bursts (black crosses, [?]) and GRB170817A. The values of E_p and L_{iso} that would have likely been measured for other viewing angles form a line in this diagram.

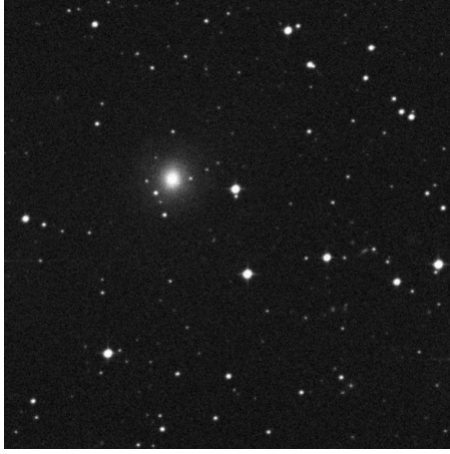


Figure 4: Time evolution of the spectrum of AT 2017gfo ([?]).

2.3 AT 2017gfo: the kilonova

2.4 The afterglow signal

3 Goal of this work and the afterglow of MMT170817 as an insight on the merger event

The merger of a binary neutron star is a complex phenomena. It most likely implies various physical components (compact objects, jets, ejectas, winds) which are subject to many dynamical and radiative processes (shock formation, nuclear processes, synchrotron emission, etc.). A coherent description of the binary neutron star merger phenomena, from the inspiral phase to the electromagnetic afterglow, is still to be found. Most likely, the combination of all the multi-messenger observations from a large number of events will be necessary to obtain this accurate description, each signal bearing the signature of the state of the phenomenon at different times.

In particular, the afterglow holds information on the state of matters at late times, and is a first step one may take to approach the event in its entirety. The goal of this work is precisely to study the afterglow of MMT170817 in the perspective of later inferring information on the earlier phases of the event: the nature and formation of the resulting compact object, the origin of the gamma ray burst, the dynamical properties of the outflow, the development of the kilonova, etc.

The questions this work addresses are thus the following:

1. What is the geometry and the structure of the matter responsible for the afterglow?

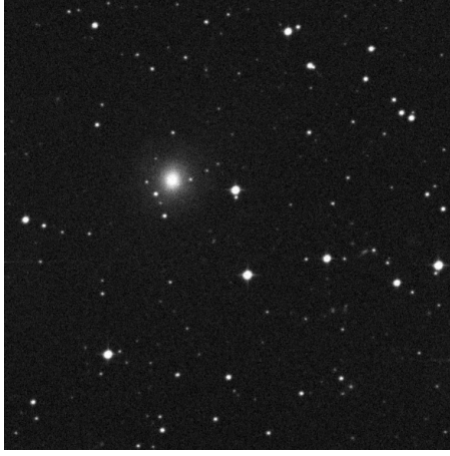


Figure 5: Some of the most long-lived afterglows from the Swift catalog (dotted lines, X-ray data), and the afterglow from MMT170817.

2. By which means is the kinetic energy dissipated into the afterglow radiation?
3. What are the characteristics of the medium in which this matter evolves?
4. Was a relativistic jet produced in the merger event?
5. By which angle do we currently see the system?
6. Which electromagnetic counterparts would we have seen, had we seen the event from different viewing angles?

Figure 6: Cut across the shock front, showing the ejected matter, and the interstellar material accumulating at the shock front.

Part II

Modelling the afterglow of MMT170817

Note on the physical origin of the afterglow. As insisted upon in the introduction, MMT170817 is an *atypical* event. Nonetheless, the numerous observations of remnants and afterglows of transient electromagnetic events (such as supernovae and gamma ray bursts) indicate a common explanation of afterglows having timescales from days to years, such as that of MMT170817. Matter which is ejected during the previous phases of the phenomenon travels in the local external medium faster than the speed of sound. A shock thus forms at the interface of this shock with the interstellar medium. Interstellar material accumulates at this shock front, is excited and radiates. As the material accumulates, the shock decelerates. The exact nature and origin of the ejected matter, and the characteristics of the medium in which it evolves depends on the specific astrophysical phenomena at hand.

Thus, the models which we will describe here and later confront to observations will concern the radiation of interstellar material which is shocked and radiates through the synchrotron process at the front of a shock formed by the piston effect of ejecta from the merger on the exterior medium, while this shock decelerates as it penetrates the ISM.

4 The physics of afterglows: deceleration dynamics, radiation and astronomical observables

In this section, we will review the physics which will take part in the modelling of the afterglow of MMT170817. We will successively describe the deceleration of the remnant expanding in the interstellar medium, the radiation of matter at the shock front, and derive the electromagnetic signals which arise from this radiation. The more technical details of these physical processes may be found in *Appendix B*.

4.1 Relativistic deceleration

We now describe the dynamics of the deceleration of the remnant in the ISM. We will consider for this work two different structures for the ejected matter: a *mono-kinetic ejecta*, or a *radially stratified ejection*.

We will follow the Lorentz factor $\Gamma(r)$ of the ejected matter once it has reached the exterior radial coordinate r .

Mono-kinetic ejection. In this case, the matter is ejected with initial energy E_0 and a single Lorentz factor Γ_0 . By plowing through the ISM, the shock sweeps up interstellar material and decelerates. By denoting M_{ej} the mass of the ejected matter, $m(r)$ the accumulated mass swept up by the shock at radius r from the point of ejection, conservation of energy implies that the initial total energy $\Gamma_0 M_{\text{ej}} c^2 + m(r) c^2$ is distributed in the ejected mass energy $\Gamma(r) M_{\text{ej}} c^2$ and the internal energy of the swept up mass $\Gamma(r)^2 m(r) c^2$. Thus:

$$\Gamma(r)^2 m(r) + \Gamma(r) M_{\text{ej}} = \Gamma_0 M_{\text{ej}} + m(r)$$

Details on the $\Gamma^2 m c^2$ form for the thermal energy of the swept-up mass can be found in *Appendix B*.

We will consider for our purposes a homogeneous medium with numeric density n .

Suppose that the mass M_{ej} was ejected into a solid angle Ω by the central source, for instance in the form of a cone. Then if we neglect any lateral expansion of the ejected matter, the swept up mass

at radius will be¹:

$$m(r) = \Omega \int_0^r dr' r'^2 n m_P$$

Thus by introducing the isotropic-equivalent ejected mass $M_{\text{iso}} = 4\pi M_{\text{ej}}/\Omega$, the dimensionless mass parameter $\mu(r) \equiv \frac{m(r)}{M_{\text{iso}}/\Gamma_0}$, writes:

$$\begin{aligned} \mu(r) &= \frac{\Omega \int_0^r dr' r'^2 n m_P}{M_{\text{ej}}/\Gamma_0} \\ &= \frac{4\pi r^3}{3M_{\text{iso}}/\Gamma_0} n m_P \end{aligned}$$

which no longer depends on the solid angle of ejection.

We may identify the *deceleration radius*, $R_{\text{dec}} = \left(\frac{3E_0}{4\pi n m_P \Gamma_0^2 c^2} \right)^{1/3}$, such that:

$$\mu(r) = \left(\frac{r}{R_{\text{dec}}} \right)^3$$

And finally, the solution for $\Gamma(r)$ is easily found to be:

$$\Gamma(r) = \Gamma_0 \frac{-1 + \sqrt{1 + 4\mu(r) + \frac{4\mu(r)^2}{\Gamma_0^2}}}{2\mu(r)}$$

Phases of deceleration. We observe three phases in the deceleration of the shock front:

1. For $\mu(r) \ll 1/4$, i.e. $r \ll R_{\text{dec}}$, in the *coasting phase*, no deceleration occurs:

$$\Gamma(r) \simeq \Gamma_0$$

2. For $1/4 \ll \mu(r) \ll \Gamma_0^2$, i.e. $R_{\text{dec}} \ll r \ll \Gamma_0^{2/3} R_{\text{dec}} \equiv R_{\text{N}}$ (*newtonian radius*), the front is in a *relativistic deceleration phase*, during which the swept-up mass progressively reaches $\Gamma_0 M$:

$$\Gamma(r) \simeq \frac{\Gamma_0}{\sqrt{\mu(r)}} = \Gamma_0 \left(\frac{r}{R_{\text{dec}}} \right)^{-3/2}$$

3. For $\Gamma_0^2 \ll \mu(r)$, i.e. $R_{\text{N}} \ll r$:

$$\Gamma(r) \simeq 1$$

and

$$\beta(r) \simeq \sqrt{\Gamma_0(\Gamma_0 - 1)} \left(\frac{r}{R_{\text{N}}} \right)^{-3/2}$$

This is the *Newtonian phase*, and we see that deceleration to non-relativistic velocities requires the sweeping up of a mass on the order of $\Gamma_0 M$.

Radially stratified structure. In this case, we suppose that the matter was ejected with an inhomogeneous distribution of velocities: some components were ejected with larger energies than others. We parametrize this distribution giving a cumulative distribution $E(> \Gamma)$ of energies. It is such that at ejection, the total energy of the matter having a Lorentz factor larger than a given $\hat{\Gamma}$ is $E(> \hat{\Gamma})$.

After the ejection, the higher-velocity component of the ejecta will form the shock front, while the rest of the ejecta lags behind. The front shock decelerating in the ISM, the slower components will catch up to the front shock. This way, the catching-up matter will slow the deceleration down, until the slowest component has caught up. Then, the dynamics are the same as a mono-kinetic ejection starting from the slowest initial velocity.

¹In all generality, we should consider the average mass per particle in the local exterior environment instead of m_P .

How to write energy conservation in this case? If the front shock has reached a Lorentz factor Γ (at r), it means that all the energy which was initially available to the ejected matter with Lorentz factors above Γ has already caught-up and been injected into the shock, since we neglect the time it takes for matter to catch-up to the shock. But the energy injected by the shock is that held in internal energy form by the swept-up material at the shock, as in the mono-kinetic ejection case. Thus, we have:

$$\Gamma(r)^2 m(r) c^2 = E(> \Gamma(r)) + m(r) c^2$$

Notice that this is an implicit equation on $\Gamma(r)$, and that we do not consider here an initial bulk mass which would have a initial energy of $\Gamma_0 M c^2$. Considering an additional bulk mass in this process would simply amount to a discontinuous function $E(> \Gamma)$.

In the case of a homogeneous medium, this reduces to:

$$\frac{4\pi}{3} r^3 n m_P c^2 (\Gamma(r)^2 - 1) = E(> \Gamma)$$

Alternatively, we parametrize the distribution in terms of the *relativistic 4-velocity* $u = \Gamma\beta$.

It follows that if the total initial energy is E_0 and the largest (resp. smallest) velocity in the ejecta is u_M (resp. u_m), then the energy distribution function can be written as:

$$E(> u) = E_0 g(u)$$

where g is a function equal to 1 for $u < u_m$, to 0 for $u_M < u$, and decreases between u_m and u_M .

The simplest functional form for g which meets these requirements is a power-law with some positive index α containing all the unknown physics of the ejection event. Explicitly, the final deceleration dynamics equation is (note that $\Gamma^2 - 1 = (\Gamma\beta)^2$):

$$\frac{4\pi r^3 n m_P c^2 u(r)^2}{3E_0} = \frac{u(r)^{-\alpha} - u_M^{-\alpha}}{u_m^{-\alpha} - u_M^{-\alpha}}$$

In this case, solving for $\Gamma(r)$ (or equivalently $u(r)$) is not analytical, and we will find $\Gamma(r)$ with help of numerical integration. For our purposes, we fix the value of α to the fiducial value of 5 ([?]).

4.2 Synchrotron radiation and self-absorption

We now turn to the radiation emerging from the shocked matter, which constitutes the afterglow emission.

From now on, we will denote with primes ' the value of quantities measured in the frame of the expanding matter, and without primes those measured in the laboratory (exterior) frame.

Shock conditions on numeric density and specific internal energy. What are the conditions at the shock front, where interstellar material is excited and radiates? They are given by the Rankine Hugoniot (e.g [?]) relations. In the case of ultrarelativistic matter (with an adiabatic index of $\gamma = 4/3$), the shock-frame numeric density and internal-to-mass energy ratio are:

$$n' = (4\Gamma + 3)n$$

and

$$\epsilon' = (\Gamma - 1)$$

Electron population and magnetic field. The physical process we consider for radiation is synchrotron radiation. The energy deposited by the shock contributes to the two factors of synchrotron radiation: a magnetic field and a population of relativistic electrons.

The microphysics of the emergence of magnetic fields in astrophysical shocks are unclear (nonetheless, see *Appendix E* for a short discussion). From our standpoint, we are concerned only with the strength of the field, and will consider that a free microphysical parameter ϵ_B relates the field magnitude to the shock-frame energy density, such that:

$$\frac{B'^2}{8\pi} = \epsilon_B n' \epsilon' m_P c^2$$

Likewise, we will consider that the electron population has a simple energy spectrum: it is a power law of index p in the Lorentz factor space as of some minimal Lorentz factor Γ_m . Note that the energy contained in the electron population is *not directional*. On the contrary to the exterior kinetic energy of the shock (emcompassed in $\Gamma(r)$), this electron energy distribution arises from an isotropic momentum distribution in the local frame, and thus may be regarded as internal energy.

We introduce yet another microphysical parameter ϵ_e , which relates the proportion of the local internal energy distribution which is carried by the electrons. By requiring that the electrons carry a fraction ϵ_e of the total internal energy, we write:

$$\int_{\gamma_m}^{\infty} d\gamma \mathcal{N}(\gamma) \gamma m_e c^2 = \epsilon_e \epsilon' m_P c^2$$

Also, normalization of the population density writes:

$$\int_{\gamma_m}^{\infty} d\gamma \mathcal{N}(\gamma) = 1$$

With an energy density $\mathcal{N}(\gamma) \propto \gamma^{-p}$, one obtains:

$$\gamma_m = \epsilon_e \frac{m_P}{m_e} \frac{p-2}{p-1} (\Gamma - 1)$$

4.3 Derivation of the astronomical observable: flux density

Emission from quasi spherical matter.

$$D(\theta, t) = \Gamma(t)(1 - \beta(t) \cos(\theta))$$

$$F^{\text{iso}}(\nu, T) = \frac{1}{4\pi D^2} \int_0^{\infty} dt \int_0^{\infty} dr \int_0^{\pi} d\theta \int_0^{2\pi} d\phi r^2 \sin \theta \frac{j'(\frac{\nu}{D(\theta, t)}, r, t) \delta\left(T - t + \frac{r \cos \theta}{c}\right)}{D(\theta, t)^2}$$

Emission from a jet seen on axis.

$$F^{\text{on}}(\nu, T, \theta_j) = \begin{cases} F^{\text{iso}}(\nu, T) & \text{if } \Gamma \theta_j \gg 1 \\ (\Gamma \theta_j)^2 F^{\text{iso}}(\nu, T) & \text{if } \Gamma \theta_j \ll 1 \end{cases}$$

Emission from a jet seen off axis.

$$F^{\text{off}}(\nu, T, \theta_j, \theta_{\text{obs}}) = a^3 F^{\text{on}}\left(\frac{\nu}{a}, aT, \theta_j\right)$$

$$a = \frac{1 - \beta(t)}{1 - \beta(t) \cos(\theta_{\text{obs}})}$$

Final parametrization. In conclusion, the overall parameters necessary to predict afterglow light curves are:

- For the external medium: n and ϵ_B ,
- For a quasi-spherical remnant: E_0 and Γ_0 in the case of a mono-kinetic ejection, or E_0 , u_m and u_M in the case of a structured ejecta,
- For a jetted ejecta: additional geometrical parameters θ_j and θ_{obs} with respect to a quasi-spherical remnant.

Figure 7: Some light curves as calculated by our model.



Figure 8: Light curves for off-axis jets as calculated with the complete integration and our simplified version. The agreement is surprisingly good, and justifies the usage of the simplified (and fast) calculation for our purposes.

4.4 An illustration of some predicted light curves

To conclude this section, we will illustrate the models with some predicted light curves.

Why does a light curve peak? dynamical or spectral regime shifts.

On the validity of the simplifications used in our study In order to evaluate the errors committed on the light curves produced by our simplified calculations (for spherical models as well as jets), some light curves on typical ranges of parameters are compared with those produced by full-fledged simulations, which do perform equal arrival time intergration in general conic geometries. Figure 4.4 reports such comparisons.

We observe the agreement to be good on the paramter ranges of interest for our study case, and we conclude that our calculations are sufficient for our purposes. Note that full-fledged calculations, albeit available, would not suite our purposes as they are slow and not fit for parameter space exploration, as we will perform in the next section.

5 The afterglow of MMT170817: modelling and results

In this section, we will answer the question: What is the geometry and the dynamical structure of the matter emitting the observed afterglow?

This will lead us to decline various hypothese regarding the deceleration regime of the remnant and its geometry in order to find a coherent description of the phenomena.

5.1 Choice and reduction of multi-wavelength data

As described earlier, the atteglow emission was detected in X-ray, radio and visible bands respectively 9, 16 and ~ 150 d post-merger (when the kilonova had sufficiently dimmed in the case of the visible band). According to our emission model, the synchrotron injection and cooling frequencies scale as the following, where the model parameters were scaled to near-best-fit values which we will infer on the following paragraphs (and $p = 2.2$):

Band	Central frequency	Wavelength
Radio	3.0 GHz	10 cm
R	4.56×10^5 GHz	657 nm
X-ray	2.42×10^8 GHz	1.23 nm

Table 1: Frequencies of the EM bands of interest for our study

Coasting phase:

$$\nu_m = 10.2 \text{ GHz} \left(\frac{\Gamma_0}{10} \right)^4 \left(\frac{n}{10^{-3} \text{ cm}^{-3}} \right)^{1/2} \left(\frac{\epsilon_B}{10^{-3}} \right)^{1/2} \left(\frac{\epsilon_e}{0.1} \right)^2 \left(\frac{\frac{p-2}{p-1}}{0.167} \right)^2$$

$$\nu_c = 9.56 \times 10^8 \text{ GHz} \left(\frac{\Gamma_0}{10} \right)^{-4} \left(\frac{n}{10^{-3} \text{ cm}^{-3}} \right)^{-3/2} \left(\frac{\epsilon_B}{10^{-3}} \right)^{-3/2} \left(\frac{t_{\text{obs}}}{10 \text{ d}} \right)^{-2}$$

Deceleraton phase:

$$\nu_m = 1.78 \times 10^{-4} \text{ Hz} \left(\frac{E_0}{10^{51} \text{ erg}} \right)^{1/2} \left(\frac{\epsilon_B}{10^{-3}} \right)^{1/2} \left(\frac{\epsilon_e}{0.1} \right)^2 \left(\frac{\frac{p-2}{p-1}}{0.167} \right)^2 \left(\frac{t_{\text{obs}}}{100 \text{ d}} \right)^{-3/2}$$

$$\nu_c = 4.38 \times 10^{21} \text{ GHz} \left(\frac{E_0}{10^{51} \text{ erg}} \right)^{-1/2} \left(\frac{n}{10^{-3} \text{ cm}^{-3}} \right)^{-1} \left(\frac{\epsilon_B}{10^{-3}} \right)^{-3/2} \left(\frac{t_{\text{obs}}}{100 \text{ d}} \right)^{-1/2}$$

Newtonian phase:

$$\nu_m = 1.46 \times 10^{-10} \text{ Hz} \left(\frac{E_0}{10^{51} \text{ erg}} \right) \left(\frac{n}{10^{-3} \text{ cm}^{-3}} \right)^{-1/2} \left(\frac{\epsilon_B}{10^{-3}} \right)^{1/2} \left(\frac{\epsilon_e}{0.1} \right)^2 \left(\frac{\frac{p-2}{p-1}}{0.167} \right)^2 \left(\frac{t_{\text{obs}}}{10^5 \text{ d}} \right)^{-1/2}$$

$$\nu_c = 1.11 \times 10^{40} \text{ GHz} \left(\frac{E_0}{10^{51} \text{ erg}} \right)^{-3/5} \left(\frac{n}{10^{-3} \text{ cm}^{-3}} \right)^{-9/10} \left(\frac{\epsilon_B}{10^{-3}} \right)^{-3/2} \left(\frac{t_{\text{obs}}}{10^5 \text{ d}} \right)^{-1/5}$$

Taking the frequencies reported in table ??, we observe that in our case, all of the frequencies of interest are within the same range of the synchrotron spectrum. Namely, in the conditions of the remnant, we have $\nu_m \ll \nu_{\text{Radio,R,X}} \ll \nu_c$ at essentially all times.

In this domain of the spectrum, the flux scales as $F_\nu \propto \nu^{\frac{1-p}{2}}$. Thus, using the entire multi-wavelength set of photometry points, one can determine the value of p once and for all, and reduce the set of points to a single band (in our case the 3 GHz band) for the rest of the study. This is done in e.g. [?], and a value of $p = 2.22 \pm 0.1$ is found.

For now on, we will take $p = 2.2$, and use the radio 3 GHz points reported in table 2. Also, we will fix the value of ϵ_e to the fiducial value of 0.1 (see e.g. [?])

5.2 Can the afterglow come from a post-GRB relativistic jet?

The first approach to solving the origin of the afterglow stems from the standard understanding of GRBs. According to this standard model (see e.g. [?], [?] sec. 5, [?]), sGRBs are produced by the dissipation of the kinetic energy of a relativistic jet into radiation by processes which are still to elucidate. As described above, the later formation of a shock front by the jet and the plowing of interstellar material decelerates the jet and leads to the decollimation of the radiation emanating from the shocked material. If the decollimation and the emitted flux are such that an exterior observer enters the emission cone, than an afterglow from the relativistic jet is observed.

We calculate light curves produced in such a manner by a mono-kinetic jet of aperture θ_j , initial kinetic energy E_j^2 and uniform Lorentz factor Γ_0 , penetrating an exterior medium of number density n and magnetic microphysical parameter ϵ_B , and observed from a angle of θ_{obs} .

²Notice that in this vision, the kinetic energy of the jet is the remainder of the jet's kinetic energy after dissipation in gamma radiation.

Time (days)	Flux (μJy)	Reference
16.42	18.7 ± 6.3	[?]
17.39	15.1 ± 3.9	—
18.33	14.5 ± 3.7	—
22.36	22.5 ± 3.4	—
24.26	25.6 ± 2.9	—
31.22	34.0 ± 3.6	[?]
46.26	44.0 ± 4	—
54.27	$48. \pm 6$	—
57.22	61.0 ± 9	—
93.13	70.0 ± 5.7	—
115.05	89.05 ± 20	—
162.89	98.0 ± 22.5	—
196.79	78.9 ± 9	[?]
216.91	$68. \pm 21$	[?]
256.76	$55. \pm 12$	—

Table 2: 3 GHz fluxes considered for our study.

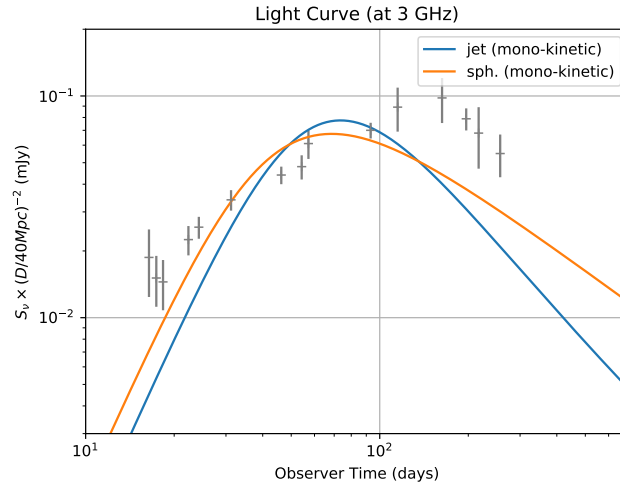


Figure 9: Best-fit light curve for the mono-kinetic jet afterglow model, and the monokinetic spherical shell model. None are an acceptable fit.

Parameter	Best-fit values (1σ confidence interval)
\bar{n}	$(8.1 \pm 1.5) \times 10^{-4} \text{cm}^{-3}$
$\bar{\epsilon}_B$	$(8.1 \pm 1.5) \times 10^{-4}$
E_0	$(5.61 \pm 0.6) \times 10^{50} \text{erg}$
\bar{u}_m	1.5 ± 0.02
\bar{u}_M	$3.19 \pm 1.$

Table 3: Best-fit parameter values for the quasi-spherical shock with radial velocity structure.

Figure 5.2 illustrates the monokinetic jet best-fit light curve to the radio points, obtained with a reduced χ^2 of $119/9 \sim 13$.

We observe that the characteristic $F(\nu, T) \propto T^3$ increase of jet afterglows does not fit the rather slow $F(\nu, T) \propto T^{0.79 \pm 0.15}$ (cf. infra) of the radio light curve. Furthermore, the smoothness of the jet afterglow peak contrasts with the strongly localized peak of the radio observations.

We may thus conclude that an acceptable fit to the radio data may not be found in the context of an afterglow produced by a post-GRB jet.

5.3 A quasi-spherical remnant

The jetted geometry for the afterglow emitter being ruled out, we now turn to the possibility that the shock front has a quasi-spherical geometry.

A mono-kinetic quasi-spherical remnant. For the same initial energies and Lorent factors, light curves from spherical and jet geometries will differ only after the jet break occurs for the jet model. Moreover, the relative weakness of the GRB hints to a likely small Lorentz factor for at least some of the matter ejected during the phenomena. Thus, we may predict that in our case of likely low Lorentz factor, spherical and jet geometry light curves of the monokinetic model will behave differently as of early times, the jet break occurring shortly for jet geometry cases.

Indeed, by adjusting only four parameters, n , ϵ_B , E_0 and Γ_0 , a better fit is found for a monokinetic spherical ejecta model, as illustrated in figure 5.2. The corresponding reduced χ^2 is $72/11 \sim 6.5$. *Nonetheless, this model is not physically realistic.*

A radially structured quasi-spherical remnant $\chi^2 = 3.97/10$

5.4 Conclusion

In conclusion, we have shown that in our model of synchrotron emission from shocked interstellar material as the origin of the afterglow of MMT170817, the most likely configuration is that the ejecta forming the shock has a quasi-spherical structure, and was ejected with a total kinetic energy of $\sim 6 \times 10^{50} \text{erg}$, with Lorentz factors in the range $\sim 2 - 3$, and it is expanding into a medium of number density $\sim 8 \times 10^{-4} \text{cm}^{-3}$ and a magnetic microphysical parameter of $\sim 1 \times 10^{-3}$. Details on the actual best-fit parameters and their confidence intervals can be found in table 3.

6 Discussion around the results from the afterglow modelling

6.1 General discussion

Degeneracy of parameters and tightness of fit. Overall, there is an important degeneracy among the parameters of the radially-structured quasi-spherical model, as indicated by the low χ^2_{red} of 0.4. Indeed, the cited best-fit values are indicative of the typical parameter to obtain the radio data, but small deviations from these best-fit values still produce acceptable light curves.

This is illustrated by studying the correlations between parameters. For the two external medium parameters n and ϵ_B , the χ^2 map projected on the (n, ϵ_B) plane around the best fit values is presented in figure 6.1. The correlation between the two variables is -0.600. Physically, a model is found to be as close to the data than the same model with a higher density and a lower magnetic parameter. This may be understood grossely by noticing that $B \propto \sqrt{\epsilon_B n}$, and thus for a same $\Gamma(r)$ (which depends on n), the emission will be equivalent by approximately conserving $\epsilon_B n$.

Similarly, we observe a strong anti-correlation between the dynamical parameter u_m and n , as shown figure ???. We observe that for u_m values smaller than best-fit, the global fitting error is

Figure 10: Projected likely-hood map on the fitting of the external parameters n and ϵ_B in the radially structured ejecta model.

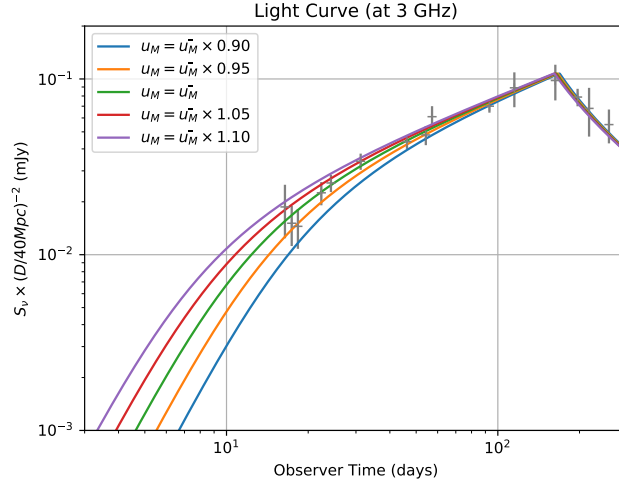


Figure 11: Radially structured model light curves with varying u_M and best-fit values for all other parameters. u_M would be better constrained with earlier flux measurements.

invariant long lines of constant $nu_m^{-\beta}$, where $\beta \sim 5 = \alpha$. Coming back to the dynamical equation ($V(r) = 4\pi r^3/3$):

$$V(r)c^2n(u_m^{-\alpha} - u_M^{-\alpha}) = E_0(u^{-\alpha} - u_M^{-\alpha})$$

It appears that if $u_m^{-\alpha} \gg u_M^{-\alpha}$, which is the case for our $\alpha = 5$ and $u_m < u_m^- \sim 1.5$, then the dynamic equation simplifies to:

$$V(r)c^2nu_m^{-\alpha} = E_0(u^{-\alpha} - u_M^{-\alpha})$$

by which the dynamics are solely determined by the product $nu_m^{-\alpha}$ as suggested by the anti-correlation we observe.

Also, we deduce from table 3 that the best-constrained parameter is u_m . As explained previously, u_m determines the moment when the dynamics switch from the catching-up phase to the monokinetic regime, consistently producing a sharp break in the dynamical behavior and thus in the light-curve. As the radio data point out, the flux features a sharp light curve maximum, and it is thus understood that the time of dynamical regime shift must be well determined and thus u_m tightly constrained.

What is the ejected matter? As we have seen, the afterglow does not likely originate from a post-GRB relativistic jet. It is more likely in a quasi-spherical shape, and was ejected with inhomogeneous velocities. This unfortunately does not inform us on the nature of this ejected matter, i.e. its composition, the process during which, when and from where it was ejected.

It may have been ejected by the friction of the two neutron stars upon coalescence, and later have formed an accretion disk around the final central object and finally been blown away by a thermal neutrino wind, producing the kilonova radiation in the process. It may also be have been emitted by an intermediate central compact object during its relaxation to its final structure as a black hole or neutron star.

It is likely that the answers to these interrogations lie in the signatures of earlier phases of the phenomenon, such as the kilonova. In particular, as illustrated in figure 6.1 and table 3, the maximum ejection velocity u_M is the most poorly constrained parameter of the radially-structured quasi-spherical model, for lack of early radio points.

Measuring radio fluxes at earlier times would allow better constraints on u_M and thus a better understanding of the ejection conditions, and therefore of the nature of the ejected matter.

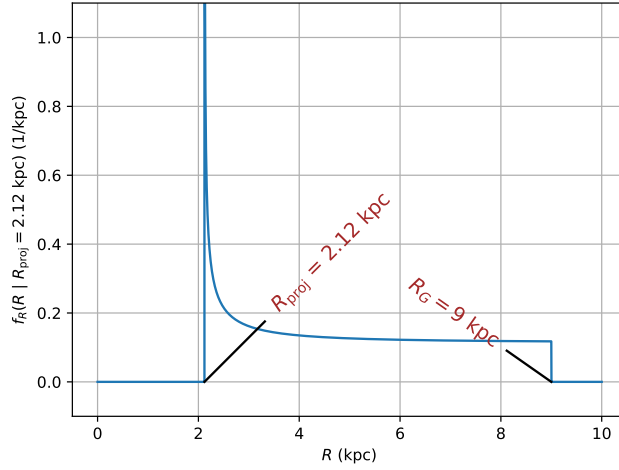


Figure 12: Probability density function for the radial distance of the merger locus to the galactic center, knowing the projected radial distance to be 2.12 kpc, and supposing the merger point drawn at random in the 9 kpc-radius galaxy.

Furthermore, it is possible that the matter currently plowing the exterior medium was not ejected simultaneously. Indeed, in the so-called *cocoon model* ([?, ?],), a relativistic jet impacts some previously ejected matter, depositing supplementary kinetic energy, and thereby *choking* the GRB. This results in no classical jet-produced GRB, but rather in a higher-energy quasi-spherical ejecta producing a weak GRB and eventually a quasi-spherical remnant and shock. Nonetheless, these models concern the origin of the shock-forming matter while our calculations are only concerned with the geometry of this matter and its final velocity distribution.

6.2 The external medium

The best-fit density parameter $\sim 10^{-3} \text{ cm}^{-3}$ value is broadly consistent with typical values inside gas-rarified early-type galaxies such as NGC4993 ([?]).

More precisely, according to recent measurements of HI 21-cm fluxes in the host galaxy of MMT170817 ([?]), an upper limit on the galactic density of atomic hydrogen is found to be $n_{\text{HI}} < 4 \times 10^{-2} \text{ cm}^{-3}$. If we suppose (as we have already done in our calculations) that the local medium is composed essentially of hydrogen, this upper limit is consistent with our model's predictions.

Similarly, with a star formation rate measured to $\sim 10^{-2} / \text{yr}$ ([?]) and using the Kennicutt-Schmidt law [?], the average density of HI in NGC4993 is estimated to $\sim 4 \times 10^{-3} \text{ cm}^{-3}$ ([?]), assuming the HI content to extend out to $\sim 18 \text{ kpc}$ from the center of NGC4993. This is roughly a factor of 2 above our prediction. As illustrated in figure 6.2, the projected position of the coalescence site is well inside the bulge of NGC4993. The angular distance from the merger site to the center of the galaxy is $\sim 10.6''$, equivalent to 2.12 kpc at 40 Mpc.

Consequently, the discrepancy in estimates of local density can be explained either by the fact that the merger site is in fact in a peripheral region of the galaxy, where the density is lower than the average, or on the contrary that the merger site is well inside the galaxy as suggested by the projected position, but the gas and dust content of NGC4993 does not follow an ordinary radially-decreasing profile. This last possibility is further supported by the presence of shell structures in NGC4993 as shown by [?], indicating a recent galactic merger event implicating the host galaxy, therefore explaining a non-trivial distribution of gas in NGC4993 and finally the possibility for lower-than-average densities even in central regions of the galaxy.

How likely is the merger site to be in the central region of NGC4993? Supposing that the merger site was drawn from a uniform distribution of points in the galaxy of radius R_G , the observation of the projected radial distance at $R_{\text{proj}} = 2.12 \text{ kpc}$ implies a posterior probability distribution for the actual radial distance R from the galactic center to the merger locus. This distribution is illustrated in fig 6.2, where we have followed [?] in taking $R_G = 9 \text{ kpc}$ (stellar extent).

We observe that the distribution is highly peaked around the projected distance, and nearly uniform

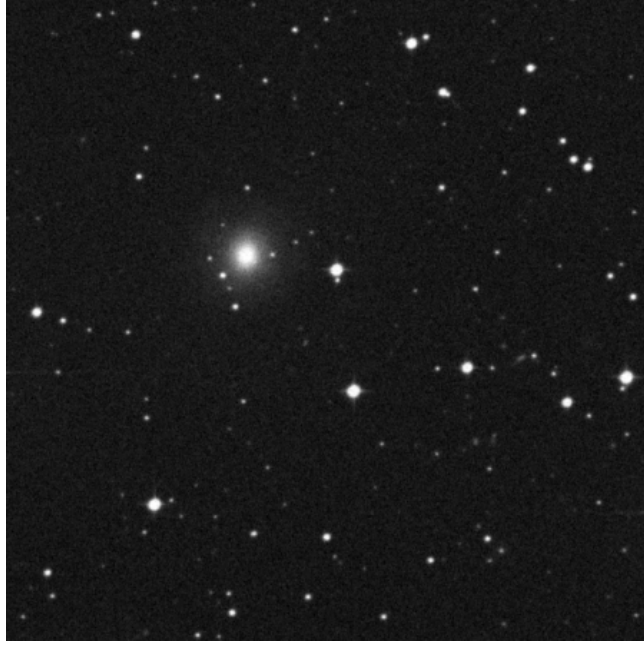


Figure 13: Localisation of the merger site as projected on the sky plane in NGC4993 ([?]).

Figure 14: Radially structured model light curves with varying exterior density n and best-fit values for other parameters.

in the rest of the density space. It is thus likely that the merger site is really in the center of the galaxy, and if it is not then no further conclusion can be drawn.

6.3 What of the standard relativistic jet?

We found in the previous section that the radio observations could not be understood as the afterglow emission from a jet-structured outflow. Nonetheless, this jet is predicted by standard model of short GRBs. The non-observation of a jet-like afterglow emission therefore constrains the characteristics of any relativistic jet which would have occurred and produced the GRB. Furthermore, if we require coherence of these constrained jets with sGRB observations and models, then constraints on the characteristics of the exterior medium are found.

What can we learn of the eventual relativistic jet from its non-observation until now?

What can we infer on the external medium by confronting these jets with sGRB observations?

Hiding the jet afterglow. How may we translate the non-observation of the jet in terms of jet afterglow time of peak and peak flux?

A first approach is to require that the jet-induced afterglow peak flux F_j^p be weaker than the observed radio flux *at the time of the jet afterglow peak* t_j^p . This of course is a weaker constraint than to require that the jet afterglow flux be *weaker than the observed fluxes at all times*. We call this the *jet hiding* condition. A mathematical formulation is:

$$F_j^p < F^{\text{obs}}(\nu, t_j^p)$$

Figure 6.3 illustrates our method to translate this into conditions in parameter space. Suppose that F_j^p and t_j^p are given in terms of a power-law on the parameters E_j , n , etc. which we will note p_1 , p_2 for now. That is:

$$F_j^p = F_0 p_1^{\alpha_1} p_2^{\alpha_2} \dots$$

and

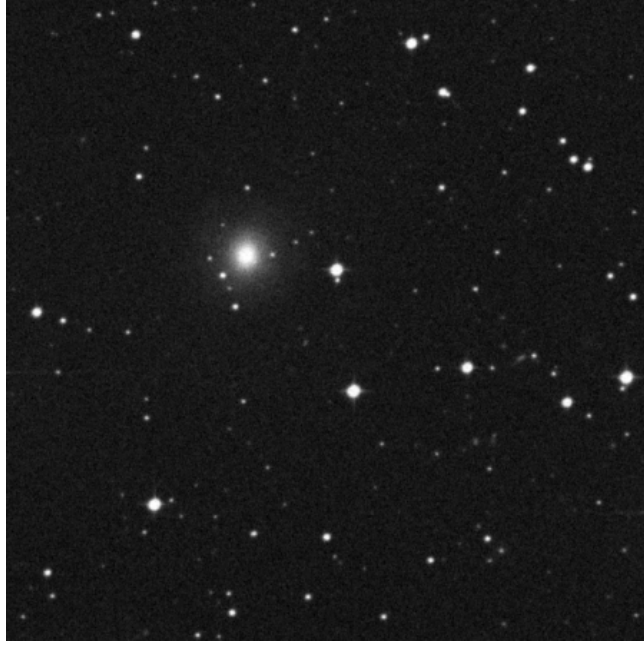


Figure 15: Illustration of the method used to obtain constraints on the relativistic jet. Changing the jet parameters will displace the maximum of the jet afterglow light curve along the vectors showed here. Requiring that the maximum be always weaker than the radio points amounts to sublinear conditions on the jet parameters.

$$t_j^p = t_0 p_1^{\beta_1} p_2^{\beta_2} \dots$$

Then, suppose that the radio light curve be given by a power law as well, that is:

$$F^{\text{obs}}(\nu, t_{\text{obs}}) = F_0^{\text{obs}} t_{\text{obs}}^{-\gamma}$$

Now, the hiding condition is thus rewritten:

$$F_0 p_1^{\alpha_1} p_2^{\alpha_2} \dots < F_0^{\text{obs}} (t_0 p_1^{\beta_1} p_2^{\beta_2} \dots)^{\gamma}$$

Which in fact results in a *sublinear condition* on the parameters for the jet to be hidden:

$$(\alpha_1 - \gamma\beta_1) \log p_1 + (\alpha_2 - \gamma\beta_2) \log p_2 + \dots < \log \left(\frac{F_0^{\text{obs}} t_0^{\gamma}}{F_0} \right)$$

The gemoetrical interpretation of this is simple: the indices α_i and β_i are just the coordinates of the vectors by which is displaced the maximum of the jet afterglow if the parameters are multiplied by 10. The hiding condition is then simply the condition on any linear combination of these vectors so that the jet remain hidden when displacing the maximum, hence changing the underlying parameters.

After a thorough exploration of the parameter space, we infer that the peak time and peak flux of a jet-induced afterglow consistently scale like the following with the jet parameters and exterior medium parameters³:

$$F_j^p = 121 \mu\text{Jy} \left(\frac{E_j}{10^{52} \text{ erg}} \right) \left(\frac{n}{10^{-3} \text{ cm}^{-3}} \right)^{4/5} \left(\frac{\epsilon_B}{10^{-3}} \right)^{4/5} \left(\frac{\theta_{\text{obs}}}{0.25 \text{ rd}} \right)^{-4.3} \left(\frac{\theta_j}{0.1 \text{ rd}} \right)^2$$

$$t_j^p = 37.4 \text{ d} \left(\frac{E_j}{10^{52} \text{ erg}} \right)^{1/3} \left(\frac{n}{10^{-3} \text{ cm}^{-3}} \right)^{-1/3} \left(\frac{\theta_{\text{obs}}}{0.25 \text{ rd}} \right)^{8/3}$$

We model the observed light curve as a broken power-law as illustrated in figure 6.3. We obtain the following:

³The initial Lorentz factor of the ejecta Γ_0 is not relevant here because as detailed in the previous section, the dynamics in the relativistic deceleration phase (during which the peak occurs) no longer depend on Γ_0



Figure 16: Superposition of the error map on the fitting of n and ϵ_B to the quasi-spherical radially structured remnant and of the sublinear constraints on these parameters obtained from the hiding of the jet.

$$F^{\text{obs}}(3 \text{ GHz}) = \begin{cases} (77.6 \pm 12.1) \mu\text{Jy} \left(\frac{t_{\text{obs}}}{100 \text{ d}} \right)^{0.791 \pm 0.152} & \text{if } t_{\text{obs}} < 163 \text{ d} \\ (45.4 \pm 41.7) \mu\text{Jy} \left(\frac{t_{\text{obs}}}{300 \text{ d}} \right)^{-1.29 \pm 1.56} & \text{if } 163 \text{ d} < t_{\text{obs}} \end{cases}$$

In conclusion, a set of jet parameters and exterior medium parameters will give rise to a hidden jet if:

$$\begin{cases} F_j^p < 77.6 \mu\text{Jy} \left(\frac{t_j^p}{100 \text{ d}} \right)^{0.791} \\ \text{and} \\ F_j^p < 45.4 \mu\text{Jy} \left(\frac{t_j^p}{300 \text{ d}} \right)^{-1.29} \end{cases}$$

taking the central values on the power-law fitting of the light curve.

In turn, this translates in parameter space to⁴:

$$\begin{cases} 0.736x_{E_j} + 1.06x_n + x_{\epsilon_B} - 5.35x_{\theta_{\text{obs}}} + 2x_{\theta_j} < -0.531 \\ \text{and} \\ 1.43x_{E_j} + 0.37x_n + x_{\epsilon_B} - 0.49x_{\theta_{\text{obs}}} + 2x_{\theta_j} < 0.74 \end{cases}$$

These are two sublinear conditions in the 5-dimensional space of jet and medium parameters which are implied by the non-observation of a jet-induced afterglow.

We will now further discuss the eventuality of a relativistic jet and constrain the external medium by specifying some values for some of the parameters in these two sublinear conditions. These values will come either from our previous results (on n and ϵ_B , coming from the fitting to the radially structured remnant light curve), or results from the gravitational wave community (on θ_{obs} mainly) or previous observations and models for GRBs (on E_j).

Further constraints on the external medium. We will now use these set of conditions to better constrain the external parameters n and ϵ_B .

⁴We introduce the notations $x_{E_j} = \log \left(\frac{E_j}{10^{52} \text{ erg}} \right)$, $x_n = \log \left(\frac{n}{10^{-3} \text{ cm}^{-3}} \right)$, $x_{\epsilon_B} = \log \left(\frac{\epsilon_B}{10^{-3}} \right)$, $x_{\theta_{\text{obs}}} = \log \left(\frac{\theta_{\text{obs}}}{0.25 \text{ rd}} \right)$, $x_{\theta_j} = \log \left(\frac{\theta_j}{0.1 \text{ rd}} \right)$.

Figure 17: Constraints on the intrinsic parameters of the relativistic jet, as visualized in the (θ_j, E_j) plane for various values of θ_{obs} below $\theta_{\text{obs}}^{\text{max}} = 28 \text{ deg}$.

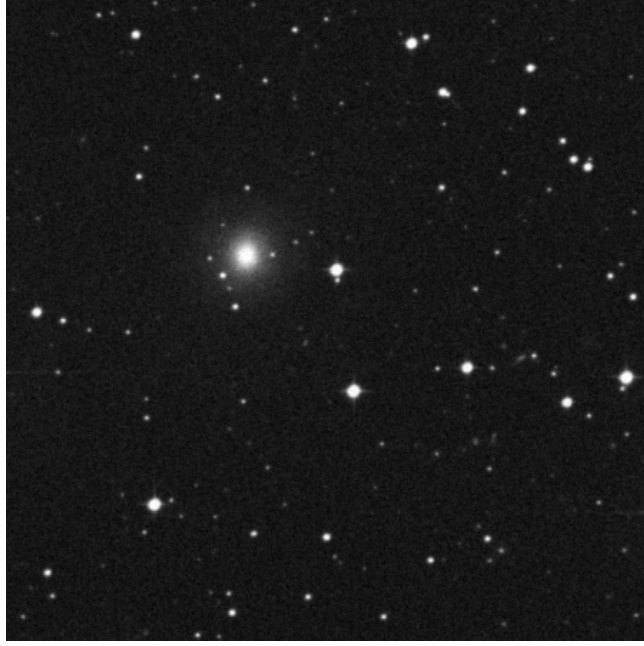


Figure 18: Afterglow light curves of jets which respect the constraints imposed by the non-observation

Discussion on the intrinsic characteristics of the jet. We now turn to constraining the intrinsic characteristics of the jet. The two sublinear conditions that we have established imply all 5 parameters of a jet afterglow. If we seek constraints on the jet parameters only (E_j, θ_j) , independently of exterior factors, then we must fix the three parameters n , ϵ_B and θ_{obs} . Likely, we have estimates for n , ϵ_B as provided by our fitting to the radially structured model which we can take. Also, we can as above vary θ_{obs} in the range indicated by the gravitational wave data from GW170817.

These constraints in the (E_j, θ_j) plane are illustrated in figure 6.3. The non-shaded region corresponds to possible hidden jets given the likely values of n and ϵ_B provided by the fitting of the afterglow with a spherical radially structured remnant.

Jet-induced bumps. Of course, our hiding condition on the maximum of the jet afterglow does not fully characterize the non-observation of a jet afterglow. Indeed, if the jet afterglow decays slower than the $t^{-1.3}$ of the radio data, than the jet can create bumps, as illustrated in figure 6.3. Thus, the parameter space which we have excluded here is in fact too loose of a constraint on the jet. In the data of MMT170817 a bump has yet to be found.

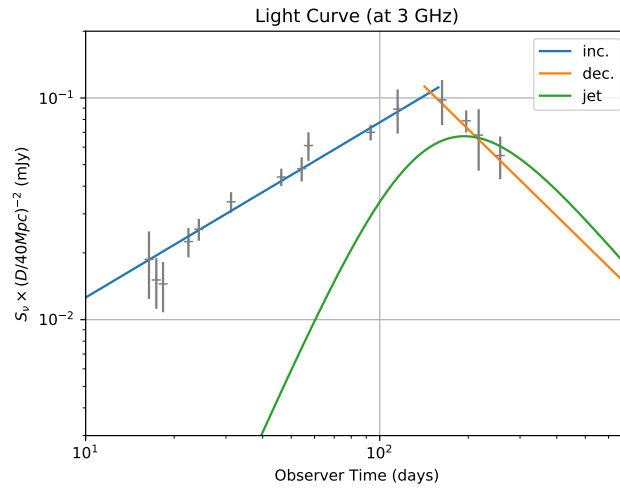


Figure 19: A jet afterglow which complies to our hiding condition (the maximum is weaker than the data at the time of maximum), yet the afterglow is clearly apparent.

Part III

Perspectives on the electromagnetic counterparts of binary neutron star mergers

7 Future rates of events and counterparts

8 Insights on other astronomical observables

In this work we were concerned with the afterglow light curve of MMT170817. As we have seen, it allows us to infer much information on the global phenomenon of neutron star mergers: from the exterior medium to the structure of the ejecta and the possibilities for a relativistic jet.

What may other astronomical observables teach us on this phenomenon?

Radio imaging of the remnant.

Polarisation of the afterglow emission. Considerations similar to those which result in the functional form of the light curve from a given distribution of emitting matter lead to

9 Open questions

What GRBs can be produced by the hidden jets? What is the nature of the resulting compact object?

What is the intrinsic diversity of the merger phenomenon?

Appendix A: Terminology

Appendix B: Details on the physics of afterglows

$$\int_0^1 dx x^2 = \frac{1}{3}$$

Appendix C: Supplementary figures

List of Figures

1	A nice figure	4
2	Spectrogram of a combination of both LIGO interferometers' data from GW170817 ([?]). Note the non-detection of a ring-down signal.	4
3	The Yonetoku relation for the Swift BAT 4 catalog bursts (black crosses, [?]) and GRB170817A. The values of E_p and L_{iso} that would have likely been measured for other viewing angles form a line in this diagram.	5
4	Time evolution of the spectrum of AT 2017gfo ([?]).	5
5	Some of the most long-lived afterglows from the Swift catalog (doted lines, X-ray data), and the afterglow from MMT170817.	6
6	Cut across the shock front, showing the ejected matter, and the interstellar material accumulating a the shock front.	7
7	Some light curves as calculated by our model.	11
8	Light curves for off-axis jets as calculated with the complete integration and our simplified version. The agreement is surprisingly good, and justifies the usage of the simplified (and fast) calculation for our purposes.	11
9	Best-fit light curve for the mono-kinetic jet afterglow model, and the monokinetic spherical shell model. None are an acceptable fit.	13
10	Projected likely-hood map on the fitting of the external parameters n and ϵ_B in the radially structured ejecta model.	15
11	Radially structured model light curves with varying u_M and best-fit values for all other paramters. u_M would be better constrained with earlier flux measurements.	15
12	Probability density function for the radial distance of the merger locus to the galactic center, knowing the projected radial distance to be 2.12 kpc, and supposing the merger point drawn at random in the 9 kpc-radius galaxy.	16
13	Localisation of the merger site as projected on the sky plane in NGC4993 ([?]).	17
14	Radially structured model light curves with varying exterior density n and best-fit values for other parameters.	17
15	Illustration of the method used to obtain constraints on the relativistic jet. Changing the jet parameters will displace the maximum of the jet afterglow light curve along the vectors showed here. Requiring that the maximum be always weaker than the radio points amounts to sublinear conditions on the jet parameters.	18
16	Superposition of the error map on the fitting of n and ϵ_B to the quasi-spherical radially structured remnant and of the sublinear constraints on these parameters obtained from the hiding of the jet.	19
17	Constraints on the intrinsic parameters of the relativistic jet, as visualized in the (θ_j, E_j) plane for various values of θ_{obs} below $\theta_{\text{obs}}^{\text{max}} = 28 \text{ deg}$	20
18	Afterglow light curves of jets which respect the constraints imposed by the non-observation	20
19	A jet afterglow which complies to our hiding condition (the maximum is weaker than the data at the time of maximum), yet the afterglow is clearly apparent.	21

List of Tables

1	Frequencies of the EM bands of interest for our study	12
2	3 GHz fluxes considered for our study.	13
3	Best-fit parameter values for the quasi-spherical shock with radial velocity structure. .	14

References

hi